# Large Exchange Bias Effect and Coverage-Dependent Interfacial Coupling in Crl<sub>3</sub>/MnBi<sub>2</sub>Te<sub>4</sub> van der Waals Heterostructures

Zhe Ying,<sup>†,#</sup> Bo Chen,<sup>†,#</sup> Chunfeng Li,<sup>†</sup> Boyuan Wei,<sup>†</sup> Zheng Dai,<sup>†</sup> Fengyi Guo,<sup>†</sup> Danfeng Pan,<sup>‡, §</sup> Haijun Zhang,<sup>†</sup> Di Wu,<sup>†</sup> Xuefeng Wang,<sup>‡</sup> Shuai Zhang,<sup>†,||,\*</sup> Fucong Fei,<sup>†,||,\*</sup> and Fengqi Song<sup>†,||,\*</sup>

<sup>†</sup>National Laboratory of Solid State Microstructures, Collaborative Innovation Center of Advanced Microstructures, and School of Physics, Nanjing University, Nanjing, 210093, China

<sup>‡</sup>National Laboratory of Solid State Microstructures, Collaborative Innovation Center of Advanced Microstructures, and School of Electronic Science and Engineering, Nanjing University, Nanjing, 210093, China

§Microfabrication and Integration Technology Center, Nanjing University, Nanjing, 210093, China

Atom Manufacturing Institute, Nanjing, 211806, China

<sup>\*</sup>These authors contributed equally to this work.

<sup>\*</sup>szhang@nju.edu.cn

<sup>\*</sup>feifucong@nju.edu.cn

<sup>\*</sup>songfengqi@nju.edu.cn

ABSTRACT: Igniting interface magnetic ordering of magnetic topological insulators by building a van der Waals heterostructure can help to reveal novel quantum states and design functional devices. Here, we observe an interesting exchange bias effect, indicating successful interfacial magnetic coupling, in CrI<sub>3</sub>/MnBi<sub>2</sub>Te<sub>4</sub> ferromagnetic insulator/antiferromagnetic topological insulator (FMI/AFM-TI) heterostructure devices. The devices originally exhibit a negative exchange bias field, which decays with increasing temperature and is unaffected by the back-gate voltage. When we change the device configuration to be half-covered by CrI<sub>3</sub>, the exchange bias becomes positive with a very large exchange bias field exceeding 300 mT. Such sensitive manipulation is explained by the competition between the FM and AFM coupling at the interface of CrI<sub>3</sub> and MnBi<sub>2</sub>Te<sub>4</sub>, pointing to coverage-dependent interfacial magnetic interactions. Our work will facilitate the development of topological and antiferromagnetic devices.

**KEYWORDS:** magnetic topological insulators, exchange bias effect, interface coupling, coverage-dependent

Since the discovery of the quantum anomalous Hall (QAH) effect in magnetically doped topological insulators (TIs), researchers have devoted considerable effort to exploring new physics with the help of this novel state <sup>1, 2</sup>. To avoid random magnetic dopants, the intrinsic antiferromagnetic (AFM) TI <sup>3-10</sup> MnBi<sub>2</sub>Te<sub>4</sub> was proposed. As a layered van der Waals (vdW) material, each MnBi<sub>2</sub>Te<sub>4</sub> layer is a septuple-layer (SL), and two neighboring layers are weakly stacked by vdW forces (the lower inset of **Figure 1b**). Within each SL, the Mn<sup>2+</sup> moments are ferromagnetically aligned along the [0001] direction, whereas Mn<sup>2+</sup> moments belonging to adjacent SLs are antiferromagnetically coupled. In subsequent experimental works, the realization of zero-field QAH state <sup>11</sup> and several other intriguing topological states <sup>12-16</sup> in exfoliated MnBi<sub>2</sub>Te<sub>4</sub> thin flakes confirmed this prediction.

However, it is suspected that the magnetic moments on the top surface of MnBi<sub>2</sub>Te<sub>4</sub> deviates from the ideal situation <sup>2, 17, 18</sup>, often resulting in the elimination of the magnetic topological gap and the absence of the QAH state. Improving the reproducibility and quality of the zero-field QAH state via surface/interface engineering of MnBi<sub>2</sub>Te<sub>4</sub> is therefore a primary objective for the community. Indeed, (magnetic) TIs proximitized by magnetic insulators <sup>19, 20</sup> or superconductors <sup>21, 22</sup> typically exhibit intriguing physical phenomena. According to the theoretical prediction, proximity to a magnetic insulator such as CrI<sub>3</sub> could facilitate the formation of the QAH state in MnBi<sub>2</sub>Te<sub>4</sub>, which results from the large exchange interaction at the interface of MnBi<sub>2</sub>Te<sub>4</sub> and CrI<sub>3</sub>. <sup>23</sup> In addition, because both MnBi<sub>2</sub>Te<sub>4</sub> and CrI<sub>3</sub> possess a sizable magnetic anisotropy with an out-of-plane easy axis <sup>3, 24-26</sup>, the heterostructure device of CrI<sub>3</sub>/MnBi<sub>2</sub>Te<sub>4</sub> is a

promising system and deserves investigation.

In this work, we fabricate FMI/AFM-TI vdW heterostructure devices of CrI<sub>3</sub>/MnBi<sub>2</sub>Te<sub>4</sub> by the dry transfer technique <sup>27-29</sup> and study their magnetotransport. Although the zero-field QAH effect is absent, the lateral shift of hysteresis loops, also known as the exchange bias effect, is successfully observed. Both negative and positive exchange bias effects are revealed by changing the interface configuration of CrI<sub>3</sub>/MnBi<sub>2</sub>Te<sub>4</sub> devices. Our work demonstrates the interesting magnetic coupling phenomenon at the interface of CrI<sub>3</sub>/MnBi<sub>2</sub>Te<sub>4</sub> and offers new insights for magnetic engineering of topological and antiferromagnetic devices.

Few-SLs MnBi<sub>2</sub>Te<sub>4</sub> and nanoflakes of CrI<sub>3</sub> have been mechanically exfoliated from their bulk crystals. After the MnBi<sub>2</sub>Te<sub>4</sub> field-effect transistor (FET) device is fabricated, the CrI<sub>3</sub>/MnBi<sub>2</sub>Te<sub>4</sub> heterostructure is formed by stacking the CrI<sub>3</sub> nanoflake on top of the MnBi<sub>2</sub>Te<sub>4</sub> device. The thickness of CrI<sub>3</sub> nanoflakes is approximately 20 nm in this study, which is thin enough to be stacked above MnBi<sub>2</sub>Te<sub>4</sub> to form an interface of satisfactory quality despite the presence of prepatterned electrodes. Meanwhile, the ~20 nm thick CrI<sub>3</sub> nanoflake can suppress thermal fluctuations and maintain a more stable magnetic anisotropy. More details about device fabrication are contained in the Experimental Methods section. **Figure 1a** shows the schematic of a CrI<sub>3</sub>/MnBi<sub>2</sub>Te<sub>4</sub> heterostructure device. As the MnBi<sub>2</sub>Te<sub>4</sub> sample is completely covered by the CrI<sub>3</sub> nanoflakes, we call this configuration as the fully-covered configuration. Graphite and hexagonal boron nitride (h-BN) flakes are used to protect the CrI<sub>3</sub> and MnBi<sub>2</sub>Te<sub>4</sub> samples from degradation <sup>24</sup>.

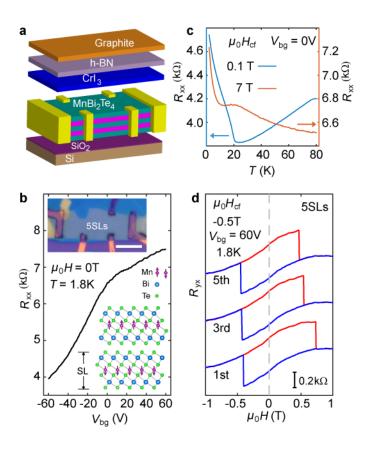


**Figure 1.** Exchange bias effect in  $CrI_3/MnBi_2Te_4$  heterostructure devices. (a) The schematic of fully-covered device configuration. (b) The  $V_{bg}$ -dependent  $R_{xx}$  of Device1 at zero magnetic field. The upper inset is the optical image of Device1. The lower inset is the atomic structure of  $MnBi_2Te_4$ . The scale bar in the top inset is 10  $\mu$ m. (c) The temperature-dependent  $R_{xx}$  curves of Device1 in field-cooling processes. (d) Exchange bias and training effects of Device1.

The upper inset of **Figure 1b** is an optical image of a  $CrI_3/(5-SLs)MnBi_2Te_4$  device (labeled Device1) before the h-BN and graphite protective layers are stacked. **Figure 1b** depicts the back-gate voltage ( $V_{bg}$ )-dependent longitudinal resistance ( $R_{xx}$ ) of Device1 at zero magnetic field, indicating that the carrier in this range is a hole type. To study the exchange bias effect, we employ the standard measurement methodology

of field-cooling treatment <sup>19, 20, 30</sup>. Given that the Curie temperature ( $T_{\rm C}$ ) of bulk CrI<sub>3</sub> and the Néel temperature ( $T_{\rm N}$ ) of MnBi<sub>2</sub>Te<sub>4</sub> crystals are 61 K and 24 K, respectively, we begin our measurement at 80 K and apply a polarizing magnetic field (cooling field,  $\mu_0 H_{\rm cf}$ ) perpendicular to the sample plane. **Figure 1c** shows the temperature-dependent  $R_{\rm xx}$  during the field-cooling processes. As previously reported, the dip or hump at ~21 K in the  $R_{\rm xx}$  -T curves represents the Néel temperature of MnBi<sub>2</sub>Te<sub>4</sub> layers <sup>11, 31</sup>. When the sample is cooled, we measure the magnetic field ( $\mu_0 H$ )-dependent Hall resistance ( $R_{\rm yx}$ ), with the  $\mu_0 H$  perpendicular to the sample plane as well. The first (1st) curve in **Figure 1d** is the typical  $R_{\rm yx}$  loop measured after field-cooling with  $\mu_0 H_{\rm cf}$  = -0.5 T of Device1, which exhibits a striking lateral shift along the horizontal axis toward the positive field. **Figure 1d** also shows the training behaviors, i.e., the exchange bias effect gradually disappears when we repeatedly sweep the hysteresis loop after field-cooling <sup>32, 33</sup>. Given the training effect, all  $R_{\rm yx}$  loops discussed in the rest of this paper are the first loop measured after the field-cooling treatment.

**Figure 2** shows detailed studies of the exchange bias effect in fully-covered CrI<sub>3</sub>/MnBi<sub>2</sub>Te<sub>4</sub> devices. As a typical FM/AFM bilayer heterostructure, CrI<sub>3</sub>/MnBi<sub>2</sub>Te<sub>4</sub> devices can serve as an ideal host for the exchange bias effect <sup>32-35</sup>, which has benefited various commercial applications <sup>32, 36</sup>. From **Figure 1d** and **Figures 2a-c**, we can determine the negative exchange bias effect by definition, <sup>19, 20</sup> since the direction of the lateral shift of the  $R_{yx}$  loop is opposite to the direction of  $\mu_0H_{cf}$ .

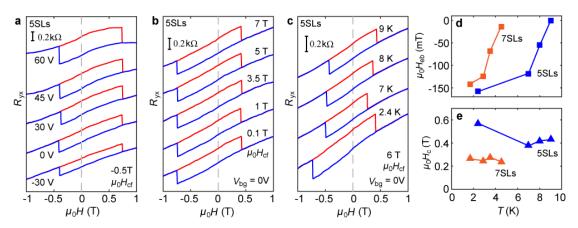
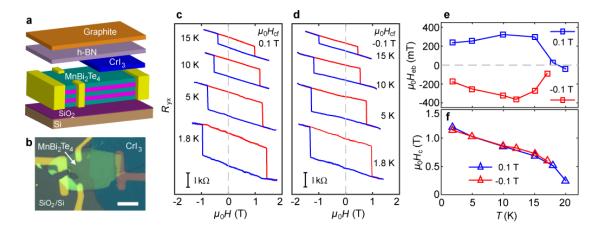


Figure 2. Back-gate voltage ( $V_{bg}$ ), cooling field ( $\mu_0H_{cf}$ ) and temperature-dependent negative exchange bias effect in fully-covered CrI<sub>3</sub>/MnBi<sub>2</sub>Te<sub>4</sub> devices. (a, b) With a certain  $\mu_0H_{cf}$  ( $V_{bg}$ ), the magnitude and sign of the exchange bias effect measured under different values of  $V_{bg}$  ( $\mu_0H_{cf}$ ) are almost unchanged in Device1. The temperature is 1.8 K. (c) The exchange bias effect at different temperatures. With increasing temperature, the exchange bias disappears gradually. (d, e) Temperature-dependent  $\mu_0H_{cb}$  (d) and  $\mu_0H_c$  (e) of different devices (Device1 and Device2) with different MnBi<sub>2</sub>Te<sub>4</sub> thicknesses.

To study whether the exchange bias field ( $\mu_0 H_{\rm cb}$  = (right coercive field + left coercive field)/2), which is a quantitative description of the lateral shift of the hysteresis loop <sup>32</sup>, <sup>35</sup>, is affected by the carrier density, we measure the exchange bias effect under different values of  $V_{\rm bg}$  (Figure 2a). Interestingly, in the  $V_{\rm bg}$  ranges that we exam,  $\mu_0 H_{\rm cb}$  shows only negligible fluctuations. Figure 2b shows the exchange bias effect of Device1 measured after field-cooling at various  $\mu_0 H_{\rm cf}$ . As  $\mu_0 H_{\rm cf}$  is positive, the resulting  $R_{\rm yx}$  loop always shifts toward a negative field, and the magnitudes of the lateral shift are quite stable, regardless of the magnitudes of  $\mu_0 H_{\rm cf}$ .

To explore the blocking temperature, i.e., the temperature above which the exchange bias effect disappears <sup>35</sup>, we carry out the measurements by varying the temperature. **Figure 2c** shows the results of Device1. The temperature-dependent  $\mu_0H_{eb}$  of Device1 is extracted and plotted in **Figure 2d**. Its blocking temperature is 9 K, which is below the Néel temperature of MnBi<sub>2</sub>Te<sub>4</sub> thin flakes (~21 K). The coercive field ( $\mu_0H_e$ ) is defined as (right coercive field – left coercive field)/2. **Figure 2e** shows the corresponding temperature dependence of  $\mu_0H_e$ . Such temperature-dependent evolution of  $\mu_0H_{eb}$  and  $\mu_0H_e$  for another heterostructure device with a MnBi<sub>2</sub>Te<sub>4</sub> thickness of 7 SLs (labeled Device2) is shown in **Figures 2d** and **2e** at the same time. See **Figure S2** for more details on Device2. Despite the obvious difference in  $\mu_0H_e$  between Device1 and Device2, the observed  $\mu_0H_{eb}$  at low temperature (~2 K) is at the same level (~-150 mT).



**Figure 3.** Positive exchange bias effect in half-covered CrI<sub>3</sub>/MnBi<sub>2</sub>Te<sub>4</sub> heterostructures. (a) The schematic of the device. (b) The optical image of Devie3 before the h-BN and graphite protective layers are stacked. The scale bar is  $10 \mu m$ . (c, d) The temperature-dependent evolution of the positive exchange bias of Device3 field cooled at 0.1 T (c) and -0.1 T (d). The  $V_{bg}$  is 0 V in these measurements. (e, f) The temperature-dependent

exchange bias field ( $\mu_0 H_{eb}$ ) and coercive field ( $\mu_0 H_c$ ) are summarized and plotted.  $\mu_0 H_{eb}$  and  $\mu_0 H_c$  of Device3 are enhanced compared to that of Device1 and Device2. The half-covered device has a higher blocking temperature.

When we change the interface configuration of CrI<sub>3</sub>/MnBi<sub>2</sub>Te<sub>4</sub> heterostructure devices by adjusting coverage approaches of CrI<sub>3</sub> nanoflake, as illustrated in Figure 3a, where only about half of MnBi<sub>2</sub>Te<sub>4</sub> is covered by CrI<sub>3</sub>, an interesting exchange bias effect appears. In particular,  $R_{yx}$  is measured on the bare MnBi<sub>2</sub>Te<sub>4</sub> region that is not covered by the CrI<sub>3</sub> layer. Figure 3b is an optical image of a fabricated device (labeled Device3), where the thickness of the MnBi<sub>2</sub>Te<sub>4</sub> layer is 8 SLs and the nearly one-half coverage is obvious. Although the MnBi<sub>2</sub>Te<sub>4</sub> thin flake is an even-layer sample in Device3, the hysteresis loop can also be observed as previously reported.<sup>6, 11, 13, 37</sup> Figures 3c and 3d show the temperature-dependent exchange bias effect of Device3 field-cooled at 0.1 T and -0.1 T, respectively. The lateral shift direction of the  $R_{\rm vx}$  loops is consistent with the direction of  $\mu_0H_{cf}$ , indicating that it is a positive exchange bias effect, 19, 20 which is in contrast to the negative exchange bias effect observed in fullycovered CrI<sub>3</sub>/MnBi<sub>2</sub>Te<sub>4</sub> devices. The extracted  $\mu_0H_{eb}$  versus temperature is plotted in Figure 3e, from which a blocking temperature of ~ 18 K can be determined, which is close to the Néel temperature of MnBi<sub>2</sub>Te<sub>4</sub> thin flakes. Remarkably,  $\mu_0 H_{\rm eb}$  could exceed 300 mT at a temperature  $\geq 10$  K. We also note that, unlike fully-covered devices, the maximum  $\mu_0 H_{\rm eb}$  does not occur at the lowest temperature for half-covered devices. The temperature-dependent  $\mu_0 H_c$  is summarized in Figure 3f as well. Obviously, both  $\mu_0 H_{eb}$ 

and  $\mu_0 H_c$  are greatly enhanced in the half-covered CrI<sub>3</sub>/MnBi<sub>2</sub>Te<sub>4</sub> devices. Similar observations can be seen in another half-covered device (labeled Device4, see **Figure S5**). It should be noted that the changes in MnBi<sub>2</sub>Te<sub>4</sub> thickness can lead to the enhancement of  $\mu_0 H_c$  as well.<sup>37</sup>

Our observations are schematically summarized in Figure 4. The exchange bias effect originates from the unidirectional anisotropy induced by the exchange interaction between the FM and AFM layers at the heterostructure interface <sup>20, 35</sup>. Generally, in FM/AFM bilayer heterostructures, the negative (positive) exchange bias effect is a result of FM (AFM) interfacial coupling, i.e., magnetic moments belonging to different materials favor FM (AFM) alignment at the interface 19, 35, 38. Based on this consideration, we conclude that the interfacial coupling in CrI<sub>3</sub>/MnBi<sub>2</sub>Te<sub>4</sub> heterostructures is coverage-dependent (or coverage-sensitive) and FM (AFM) type in fully-covered (half-covered) configuration (Figure 4a-c). Although FM type interfacial coupling always demonstrates a negative exchange bias effect, AFM type interfacial coupling typically demonstrates a positive (negative) exchange bias effect when the  $\mu_0 H_{\rm cf}$  is high (low). <sup>19,38</sup> In the field-cooling process, the FM ordering of CrI<sub>3</sub> is formed as the temperature is lower than  $\sim 61$  K. When the temperature is further lower than ~21 K, the surface spins of MnBi<sub>2</sub>Te<sub>4</sub> will be ordered parallel to those of CrI<sub>3</sub> due to FM type coupling in fully-covered situation (Figure 4a). However, the surface spins of MnBi<sub>2</sub>Te<sub>4</sub> can be ordered differently in half-covered situation. When  $\mu_0H_{\rm cf}$  is low, the exchange coupling energy between the FM and AFM layer predominates over the Zeeman energy induced by  $\mu_0 H_{\rm cf}$  and vice versa. <sup>19</sup> Therefore, below ~21 K, the surface

spins of MnBi<sub>2</sub>Te<sub>4</sub> can be ordered antiparallel (parallel) to those of CrI<sub>3</sub> with a low (high)  $\mu_0H_{cf}$  (**Figure 4b, c**). But we cannot conclude from our experiments that the MnBi<sub>2</sub>Te<sub>4</sub> surface spins can be perfectly aligned out of plane, so we use hollow arrows to represent them. Observations of a negative exchange bias effect in fully-covered CrI<sub>3</sub>/MnBi<sub>2</sub>Te<sub>4</sub> devices and a positive exchange bias effect in half-covered devices correspond to the situation of **Figures 4a** and **4c**, respectively. In the control experiment of another half-covered device (Device4), we also observed the situation of **Figure 4b** (for more details, see **Figure S6**).

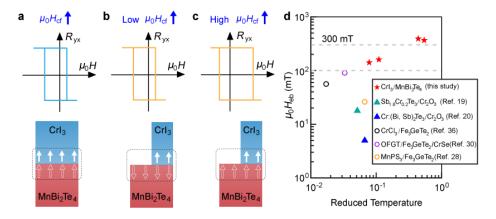


**Figure 4.** Coverage-dependent interfacial coupling and exchange bias effect with large  $\mu_0H_{eb}$  in CrI<sub>3</sub>/MnBi<sub>2</sub>Te<sub>4</sub> heterostructures. (a-c) Negative and positive exchange bias effects are observed in CrI<sub>3</sub>/MnBi<sub>2</sub>Te<sub>4</sub> heterostructures of different configurations, i.e., fully-covered (a) and half-covered (c) configurations. The simplistic illustrations of spin textures at the interface after field-cooling are shown as well. In the fully-covered (half-covered) device configuration, the spins of CrI<sub>3</sub> and MnBi<sub>2</sub>Te<sub>4</sub> prefer FM (AFM) coupling at the interface. In a half-covered device configuration, as a result of AFM interfacial coupling strength competing against the Zeeman energy that originates from

 $\mu_0 H_{cf}$ , the field-cooling processes with low  $\mu_0 H_{cf}$  (b) and high  $\mu_0 H_{cf}$  (c) can lead to different interfacial spin textures and exchange bias behavior. (d) The  $\mu_0 H_{eb}$  observed in this study and several other works are plotted. The four points of this study are the results of Device1-Device4 in the main text. The solid symbols are TIs related.

We note that the exchange bias effect reported in this study is revealed in the AFM layer (MnBi<sub>2</sub>Te<sub>4</sub> here), which differs from usual circumstances <sup>19, 20, 30, 35, 36</sup>. The large  $\mu_0H_{eb}$  observed in the CrI<sub>3</sub>/MnBi<sub>2</sub>Te<sub>4</sub> heterostructure is outstanding compared with several other vdW FM/AFM heterostructures studied in recent years. In **Figure 4d**, we provide a comparison of the  $\mu_0H_{eb}$  observed in other works. As these works also measure  $R_{yx}$ , we define a reduced temperature as the measurement temperature divided by the Curie (or Néel) temperature of the material that contributes to the  $R_{yx}$  signal. An alternative definition of the reduced temperature would be the measurement temperature divided by the blocking temperature, as suggested in **ref 35**. Since the blocking temperature is not explored in all prior studies, our definition is reasonable and informative for a qualitative comparison. Obviously, the large  $\mu_0H_{eb}$  observed in CrI<sub>3</sub>/MnBi<sub>2</sub>Te<sub>4</sub> vdW heterostructures is striking.

These large  $\mu_0 H_{eb}$  and coverage-dependent interfacial interactions are explained by the competitive onset of FM and AFM coupling at the interface of CrI<sub>3</sub> and MnBi<sub>2</sub>Te<sub>4</sub>. Generally, interfacial coupling is either FM-type or AFM-type <sup>19, 35</sup>. However, the energy discrepancy between the FM and AFM interfacial coupling can sometimes be small, resulting in competitive switching between negative and positive exchange bias

effects, as reported in protonic-gate-tuned oxidized Fe<sub>3</sub>GeTe<sub>2</sub> nanoflakes <sup>39</sup>. For the CrI<sub>3</sub>/MnBi<sub>2</sub>Te<sub>4</sub> heterostructures studied here, FM coupling would be more favorable <sup>23</sup>. Therefore, in the fully-covered configuration, FM interfacial coupling and thus a negative exchange bias effect are anticipated. Although AFM coupling requires a higher energy in a fully-covered configuration, it is possible in a half-covered configuration because the competition between FM and AFM coupling is sensitive to interface details <sup>40</sup> and can be controlled. The larger  $\mu_0 H_{eb}$  in half-covered devices may indicate that the AFM coupling in this configuration is stronger than the FM coupling in the fully-covered configuration <sup>32,35</sup>. The FM and AFM coupling competition picture helps us to understand our observations and suggests that minor changes at the interface of FM/AFM heterostructures can result in remarkable improvements in device performance.

One may also suspect that these observations are caused by stray fields  $^{41}$  of the CrI<sub>3</sub> layer. In half-covered devices, the stray fields of the CrI<sub>3</sub> layer experienced by bare MnBi<sub>2</sub>Te<sub>4</sub> region and CrI<sub>3</sub>-covered MnBi<sub>2</sub>Te<sub>4</sub> region have opposite directions. Such an explanation is ruled out by our control experiment in Device4, where the  $R_{yx}$  of bare MnBi<sub>2</sub>Te<sub>4</sub> region and CrI<sub>3</sub>-covered MnBi<sub>2</sub>Te<sub>4</sub> region are probed simultaneously. A positive exchange bias effect is observed in both regions. Moreover, the two regions have identical coercive fields and  $\mu_0H_{eb}$  (see **Figure S5** for more details). This leads us to believe that the entire MnBi<sub>2</sub>Te<sub>4</sub> layer is uniformly biased. In addition, given the smaller coercive field of CrI<sub>3</sub> compared to that of MnBi<sub>2</sub>Te<sub>4</sub>, it is unlikely that the stray fields of CrI<sub>3</sub> can bias the hysteresis loop of MnBi<sub>2</sub>Te<sub>4</sub>.

In summary, we demonstrate the interesting exchange bias effect in  $CrI_3/MnBi_2Te_4$  vdW heterostructure devices. Depending on the heterostructure configuration, fully-covered and half-covered  $CrI_3/MnBi_2Te_4$  devices exhibit negative and positive exchange bias effects, respectively. This coverage-dependent proximity approach for magnetic engineering would also work in other magnetic vdW heterostructures and deserves further investigation. The magneto-optical imaging techniques such as reflective magnetic circular dichroism (RMCD) imaging would provide a deeper comprehension of the observations here in the future. The large  $\mu_0H_{eb}$  in our experiment confirms the efficient interfacial coupling of  $CrI_3$  and  $MnBi_2Te_4$ . Our work will facilitate the development of antiferromagnetic and  $TI_3$ -based spintronics. <sup>42</sup>

#### **EXPERIMENTAL METHODS**

**Device Fabrication.** MnBi<sub>2</sub>Te<sub>4</sub> bulk crystals were grown by the flux method as previously reported.<sup>6</sup> High-quality CrI<sub>3</sub> crystals were synthesized by a chemical vapor transport method using iodine (I<sub>2</sub>) as a transport agent. Few-SLs MnBi<sub>2</sub>Te<sub>4</sub> and thin flakes of CrI<sub>3</sub> (h-BN, graphite) were mechanically exfoliated onto 300-nm-thick SiO<sub>2</sub>/Si substrate and polydimethylsiloxane (PDMS) substrate, respectively. The electrode pattern was defined by electron beam lithography, and then the Au film was evaporated to form electrical contact. After the lift-off process, the MnBi<sub>2</sub>Te<sub>4</sub> FET device was sequentially covered by pre-exfoliated CrI<sub>3</sub>, h-BN and graphite flakes. Most fabrication processes were carried out in a glove box with H<sub>2</sub>O and O<sub>2</sub> levels below 0.1 ppm.

**Transport Measurements.** The electrical transport measurements were conducted in a cryostat (1.6 K, 12 T), with the magnetic field applied perpendicular to the sample plane. The longitudinal resistance  $R_{xx}$  and Hall resistance  $R_{yx}$  were measured using standard lock-in technique with an a.c. excitation current of 50 nA at 13 Hz. The  $R_{yx}$  data shown in **Figures 3c** and **3d** in the main text were anti-symmetrized to eliminate the mixing of  $R_{yx}$  and  $R_{xx}$  signals induced by the irregular sample geometry. <sup>11</sup>, <sup>36</sup> All other  $R_{yx}$  data shown in the main text and **Supporting Information** are raw data, unless pointed out otherwise.

## ASSOCIATED CONTENT Supporting Information

The  $R_{yx}$  curve of Device1 under high magnetic field; Chern insulator state and negative exchange bias effect of another fully-covered CrI<sub>3</sub>/MnBi<sub>2</sub>Te<sub>4</sub> heterostructure device (Device2); the  $R_{yx}$  curve of Device3 under high magnetic field; the raw data of Figures 3c and 3d; details of the positive exchange bias effect observed in Device4; the negative exchange bias effect in half-covered device field cooled at low  $\mu_0 H_{cf}$ , i.e., the situation of Figure 4b; transport results in a CrI<sub>3</sub>/MnBi<sub>2</sub>Te<sub>4</sub> heterostructure device with a CrI<sub>3</sub>-coverage between full-cover and half-cover.

#### **Author contributions**

Z.Y. and B.C. contributed equally to this work. F.S., S.Z. and F.F. supervised the project. Z.Y. developed the heterostructure devices and performed the measurements. B.C. synthesized the crystals. Z.Y., S.Z., F.S., F.F., X.W., D.W. and H.Z. performed data

analysis and discussion. Z.Y., S.Z. and F.S. wrote the paper with the help from all coauthors.

### **Notes**

The authors declare no competing interests.

The data sets generated and/or analyzed during this study are available from the corresponding author upon reasonable request.

### **ACKNOWLEDGEMENTS**

We gratefully acknowledge the financial support of the National Key R&D Program of China (No. 2022YFA1402404), the National Natural Science Foundation of China (Grant Nos. 92161201, T2221003, 12104221, 12025404, 12004174, 11904166, 11904165, 12274208, 61822403, and 11874203), the Natural Science Foundation of Jiangsu Province (Grant Nos. BK20200312 and BK20200310), and the Fundamental Research Funds for the Central Universities (Nos. 020414380192).

### **REFERENCES**

- 1. Chang, C.-Z.; Zhang, J.; Feng, X.; Shen, J.; Zhang, Z.; Guo, M.; Li, K.; Ou, Y.; Wei, P.; Wang, L.-L.; Ji, Z.-Q.; Feng, Y.; Ji, S.; Chen, X.; Jia, J.; Dai, X.; Fang, Z.; Zhang, S.-C.; He, K.; Wang, Y.; Lu, L.; Ma, X.-C.; Xue, Q.-K. Experimental Observation of the Quantum Anomalous Hall Effect in a Magnetic Topological Insulator. *Science* **2013**, 340 (6129), 167-170.
- 2. Chang, C.-Z.; Liu, C.-X.; MacDonald, A. H., Quantum anomalous Hall effect. arXiv:2202.13902.
- 3. Otrokov, M. M.; Klimovskikh, I. I.; Bentmann, H.; Estyunin, D.; Zeugner, A.; Aliev, Z. S.; Gaß, S.; Wolter, A. U. B.; Koroleva, A. V.; Shikin, A. M.; Blanco-Rey, M.; Hoffmann, M.; Rusinov, I. P.; Vyazovskaya, A. Y.; Eremeev, S. V.; Koroteev, Y. M.; Kuznetsov, V. M.; Freyse, F.; Sánchez-Barriga, J.; Amiraslanov, I. R.; Babanly, M. B.; Mamedov, N. T.; Abdullayev, N. A.; Zverev, V. N.; Alfonsov, A.; Kataev, V.; Büchner, B.; Schwier, E. F.; Kumar, S.; Kimura, A.; Petaccia, L.; Di Santo, G.; Vidal, R. C.; Schatz, S.; Kißner, K.; Ünzelmann, M.; Min, C. H.; Moser, S.; Peixoto, T. R. F.; Reinert, F.; Ernst, A.; Echenique, P. M.; Isaeva, A.; Chulkov, E. V. Prediction and observation of an antiferromagnetic topological insulator. *Nature* **2019**, 576 (7787), 416-422.
- 4. Gong, Y.; Guo, J.; Li, J.; Zhu, K.; Liao, M.; Liu, X.; Zhang, Q.; Gu, L.; Tang, L.; Feng, X.; Zhang, D.; Li, W.; Song, C.; Wang, L.; Yu, P.; Chen, X.; Wang, Y.; Yao, H.; Duan, W.; Xu, Y.; Zhang, S.-C.; Ma, X.; Xue, Q.-K.; He, K. Experimental Realization of an Intrinsic Magnetic Topological Insulator. *Chin. Phys. Lett.* **2019**, 36 (7), 076801.
- 5. Pei, C.; Xia, Y.; Wu, J.; Zhao, Y.; Gao, L.; Ying, T.; Gao, B.; Li, N.; Yang, W.; Zhang, D.; Gou, H.; Chen, Y.; Hosono, H.; Li, G.; Qi, Y. Pressure-Induced Topological and Structural Phase Transitions in an Antiferromagnetic Topological Insulator. *Chin. Phys. Lett.* **2020**, 37 (6), 066401.
- 6. Chen, B.; Fei, F.; Zhang, D.; Zhang, B.; Liu, W.; Zhang, S.; Wang, P.; Wei, B.; Zhang, Y.; Zuo, Z.; Guo, J.; Liu, Q.; Wang, Z.; Wu, X.; Zong, J.; Xie, X.; Chen, W.; Sun, Z.; Wang, S.; Zhang, Y.; Zhang, M.; Wang, X.; Song, F.; Zhang, H.; Shen, D.; Wang, B. Intrinsic magnetic topological insulator phases in the Sb doped MnBi<sub>2</sub>Te<sub>4</sub> bulks and thin flakes. *Nat. Commun.* **2019**, 10 (1), 4469.
- 7. Li, J.; Li, Y.; Du, S.; Wang, Z.; Gu, B.-L.; Zhang, S.-C.; He, K.; Duan, W.; Xu, Y. Intrinsic magnetic topological insulators in van der Waals layered MnBi<sub>2</sub>Te<sub>4</sub>-family materials. *Sci. Adv.* **2019**, 5 (6), eaaw5685.
- 8. Rienks, E. D. L.; Wimmer, S.; Sánchez-Barriga, J.; Caha, O.; Mandal, P. S.; Růžička, J.; Ney, A.; Steiner, H.; Volobuev, V. V.; Groiss, H.; Albu, M.; Kothleitner, G.; Michalička, J.; Khan, S. A.; Minár, J.; Ebert, H.; Bauer, G.; Freyse, F.; Varykhalov, A.; Rader, O.; Springholz, G. Large magnetic gap at the Dirac point in Bi<sub>2</sub>Te<sub>3</sub>/MnBi<sub>2</sub>Te<sub>4</sub> heterostructures. *Nature* **2019**, 576 (7787), 423-428.
- 9. Otrokov, M. M.; Rusinov, I. P.; Blanco-Rey, M.; Hoffmann, M.; Vyazovskaya, A. Y.; Eremeev, S. V.; Ernst, A.; Echenique, P. M.; Arnau, A.; Chulkov, E. V. Unique Thickness-Dependent Properties of the van der Waals Interlayer Antiferromagnet MnBi<sub>2</sub>Te<sub>4</sub> Films. *Phys. Rev. Lett.* **2019**, 122 (10), 107202.
- 10. Ji, H.-R.; Liu, Y.-Z.; Wang, H.; Luo, J.-W.; Li, J.-H.; Li, H.; Wu, Y.; Xu, Y.; Wang,

- J. Detection of Magnetic Gap in Topological Surface States of MnBi<sub>2</sub>Te<sub>4</sub>. *Chin. Phys. Lett.* **2021**, 38 (10), 107404.
- 11. Deng, Y.; Yu, Y.; Shi Meng, Z.; Guo, Z.; Xu, Z.; Wang, J.; Chen Xian, H.; Zhang, Y. Quantum anomalous Hall effect in intrinsic magnetic topological insulator MnBi<sub>2</sub>Te<sub>4</sub>. *Science* **2020**, 367 (6480), 895-900.
- 12. Ge, J.; Liu, Y.; Li, J.; Li, H.; Luo, T.; Wu, Y.; Xu, Y.; Wang, J. High-Chern-number and high-temperature quantum Hall effect without Landau levels. *Natl. Sci. Rev.* **2020**, 7 (8), 1280-1287.
- 13. Ovchinnikov, D.; Huang, X.; Lin, Z.; Fei, Z.; Cai, J.; Song, T.; He, M.; Jiang, Q.; Wang, C.; Li, H.; Wang, Y.; Wu, Y.; Xiao, D.; Chu, J.-H.; Yan, J.; Chang, C.-Z.; Cui, Y.-T.; Xu, X. Intertwined Topological and Magnetic Orders in Atomically Thin Chern Insulator MnBi<sub>2</sub>Te<sub>4</sub>. *Nano Lett.* **2021**, 21 (6), 2544-2550.
- 14. Gao, A.; Liu, Y.-F.; Hu, C.; Qiu, J.-X.; Tzschaschel, C.; Ghosh, B.; Ho, S.-C.; Bérubé, D.; Chen, R.; Sun, H.; Zhang, Z.; Zhang, X.-Y.; Wang, Y.-X.; Wang, N.; Huang, Z.; Felser, C.; Agarwal, A.; Ding, T.; Tien, H.-J.; Akey, A.; Gardener, J.; Singh, B.; Watanabe, K.; Taniguchi, T.; Burch, K. S.; Bell, D. C.; Zhou, B. B.; Gao, W.; Lu, H.-Z.; Bansil, A.; Lin, H.; Chang, T.-R.; Fu, L.; Ma, Q.; Ni, N.; Xu, S.-Y. Layer Hall effect in a 2D topological axion antiferromagnet. *Nature* **2021**, 595 (7868), 521-525.
- 15. Ying, Z.; Zhang, S.; Chen, B.; Jia, B.; Fei, F.; Zhang, M.; Zhang, H.; Wang, X.; Song, F. Experimental evidence for dissipationless transport of the chiral edge state of the high-field Chern insulator in MnBi<sub>2</sub>Te<sub>4</sub> nanodevices. *Phys. Rev. B* **2022**, 105 (8), 085412.
- 16. Liu, C.; Wang, Y.; Li, H.; Wu, Y.; Li, Y.; Li, J.; He, K.; Xu, Y.; Zhang, J.; Wang, Y. Robust axion insulator and Chern insulator phases in a two-dimensional antiferromagnetic topological insulator. *Nat. Mater.* **2020,** 19 (5), 522-527.
- 17. Hao, Y.-J.; Liu, P.; Feng, Y.; Ma, X.-M.; Schwier, E. F.; Arita, M.; Kumar, S.; Hu, C.; Lu, R. e.; Zeng, M.; Wang, Y.; Hao, Z.; Sun, H.-Y.; Zhang, K.; Mei, J.; Ni, N.; Wu, L.; Shimada, K.; Chen, C.; Liu, Q.; Liu, C. Gapless Surface Dirac Cone in Antiferromagnetic Topological Insulator MnBi<sub>2</sub>Te<sub>4</sub>. *Phys. Rev. X* **2019**, 9 (4), 041038. 18. Swatek, P.; Wu, Y.; Wang, L.-L.; Lee, K.; Schrunk, B.; Yan, J.; Kaminski, A. Gapless Dirac surface states in the antiferromagnetic topological insulator MnBi<sub>2</sub>Te<sub>4</sub>. *Phys. Rev. B* **2020**, 101 (16), 161109.
- 19. Wang, F.; Xiao, D.; Yuan, W.; Jiang, J.; Zhao, Y.-F.; Zhang, L.; Yao, Y.; Liu, W.; Zhang, Z.; Liu, C.; Shi, J.; Han, W.; Chan, M. H. W.; Samarth, N.; Chang, C.-Z. Observation of Interfacial Antiferromagnetic Coupling between Magnetic Topological Insulator and Antiferromagnetic Insulator. *Nano Lett.* **2019**, 19 (5), 2945-2952.
- 20. Pan, L.; Grutter, A.; Zhang, P.; Che, X.; Nozaki, T.; Stern, A.; Street, M.; Zhang, B.; Casas, B.; He, Q. L.; Choi, E. S.; Disseler, S. M.; Gilbert, D. A.; Yin, G.; Shao, Q.; Deng, P.; Wu, Y.; Liu, X.; Kou, X.; Masashi, S.; Han, X.; Binek, C.; Chambers, S.; Xia, J.; Wang, K. L. Observation of Quantum Anomalous Hall Effect and Exchange Interaction in Topological Insulator/Antiferromagnet Heterostructure. *Adv. Mater.* **2020**, 32 (34), 2001460.
- 21. Xu, W.-Z.; Chu, C.-G.; Pan, Z.-C.; Chen, J.-J.; Wang, A.-Q.; Tan, Z.-B.; Zhu, P.-F.; Ye, X.-G.; Yu, D.-P.; Liao, Z.-M. Proximity-induced superconducting gap in the

- intrinsic magnetic topological insulator MnBi<sub>2</sub>Te<sub>4</sub>. Phys. Rev. B 2022, 105 (18), 184515.
- 22. Zhu, Z.; Papaj, M.; Nie, X.-A.; Xu, H.-K.; Gu, Y.-S.; Yang, X.; Guan, D.; Wang,
- S.; Li, Y.; Liu, C.; Luo, J.; Xu, Z.-A.; Zheng, H.; Fu, L.; Jia, J.-F. Discovery of segmented Fermi surface induced by Cooper pair momentum. *Science* **2021**, 374 (6573), 1381-1385.
- 23. Fu, H.; Liu, C.-X.; Yan, B. Exchange bias and quantum anomalous Hall effect in the MnBi<sub>2</sub>Te<sub>4</sub>/CrI<sub>3</sub> heterostructure. *Sci. Adv.* **2020,** 6 (10), eaaz0948.
- 24. Gong, C.; Zhang, X. Two-dimensional magnetic crystals and emergent heterostructure devices. *Science* **2019**, 363 (6428), eaav4450.
- 25. Huang, B.; Clark, G.; Navarro-Moratalla, E.; Klein, D. R.; Cheng, R.; Seyler, K. L.; Zhong, D.; Schmidgall, E.; McGuire, M. A.; Cobden, D. H.; Yao, W.; Xiao, D.; Jarillo-Herrero, P.; Xu, X. Layer-dependent ferromagnetism in a van der Waals crystal down to the monolayer limit. *Nature* **2017**, 546 (7657), 270-273.
- 26. Mak, K. F.; Shan, J.; Ralph, D. C. Probing and controlling magnetic states in 2D layered magnetic materials. *Nat. Rev. Phys.* **2019**, 1 (11), 646-661.
- 27. Castellanos-Gomez, A.; Buscema, M.; Molenaar, R.; Singh, V.; Janssen, L.; van der Zant, H. S. J.; Steele, G. A. Deterministic transfer of two-dimensional materials by all-dry viscoelastic stamping. *2D Mater.* **2014,** 1 (1), 011002.
- 28. Hu, G.; Zhu, Y.; Xiang, J.; Yang, T.-Y.; Huang, M.; Wang, Z.; Wang, Z.; Liu, P.; Zhang, Y.; Feng, C.; Hou, D.; Zhu, W.; Gu, M.; Hsu, C.-H.; Chuang, F.-C.; Lu, Y.; Xiang, B.; Chueh, Y.-L. Antisymmetric Magnetoresistance in a van der Waals Antiferromagnetic/Ferromagnetic Layered MnPS<sub>3</sub>/Fe<sub>3</sub>GeTe<sub>2</sub> Stacking Heterostructure. *ACS Nano* **2020**, 14 (9), 12037-12044.
- 29. Dai, H.; Cheng, H.; Cai, M.; Hao, Q.; Xing, Y.; Chen, H.; Chen, X.; Wang, X.; Han, J.-B. Enhancement of the Coercive Field and Exchange Bias Effect in Fe<sub>3</sub>GeTe<sub>2</sub>/MnPX<sub>3</sub> (X = S and Se) van der Waals Heterostructures. *ACS Appl. Mater.* **2021**, 13 (20), 24314-24320.
- 30. Wu, Y.; Wang, W.; Pan, L.; Wang, K. L. Manipulating Exchange Bias in a Van der Waals Ferromagnet. *Adv. Mater.* **2022**, 34 (12), 2105266.
- 31. Zhang, S.; Wang, R.; Wang, X.; Wei, B.; Chen, B.; Wang, H.; Shi, G.; Wang, F.; Jia, B.; Ouyang, Y.; Xie, F.; Fei, F.; Zhang, M.; Wang, X.; Wu, D.; Wan, X.; Song, F.; Zhang, H.; Wang, B. Experimental Observation of the Gate-Controlled Reversal of the Anomalous Hall Effect in the Intrinsic Magnetic Topological Insulator MnBi<sub>2</sub>Te<sub>4</sub> Device. *Nano Lett.* **2020,** 20 (1), 709-714.
- 32. Kiwi, M. Exchange bias theory. J. Magn. Magn. Mater. 2001, 234 (3), 584-595.
- 33. Manna, P. K.; Yusuf, S. M. Two interface effects: Exchange bias and magnetic proximity. *Phys. Rep.* **2014**, 535 (2), 61-99.
- 34. Meiklejohn, W. H.; Bean, C. P. New Magnetic Anisotropy. *Phys. Rev.* **1956,** 102 (5), 1413-1414.
- 35. Nogués, J.; Schuller, I. K. Exchange bias. *J. Magn. Magn. Mater.* **1999,** 192 (2), 203-232.
- 36. Zhu, R.; Zhang, W.; Shen, W.; Wong, P. K. J.; Wang, Q.; Liang, Q.; Tian, Z.; Zhai, Y.; Qiu, C.-w.; Wee, A. T. S. Exchange Bias in van der Waals CrCl<sub>3</sub>/Fe<sub>3</sub>GeTe<sub>2</sub> Heterostructures. *Nano Lett.* **2020,** 20 (7), 5030-5035.

- 37. Yang, S.; Xu, X.; Zhu, Y.; Niu, R.; Xu, C.; Peng, Y.; Cheng, X.; Jia, X.; Huang, Y.; Xu, X.; Lu, J.; Ye, Y. Odd-Even Layer-Number Effect and Layer-Dependent Magnetic Phase Diagrams in MnBi<sub>2</sub>Te<sub>4</sub>. *Phys. Rev. X* **2021**, 11, (1), 011003.
- 38. Nogués, J.; Leighton, C.; Schuller, I. K. Correlation between antiferromagnetic interface coupling and positive exchange bias. *Phys. Rev. B* **2000**, 61 (2), 1315-1317.
- 39. Zheng, G.; Xie, W.-Q.; Albarakati, S.; Algarni, M.; Tan, C.; Wang, Y.; Peng, J.; Partridge, J.; Farrar, L.; Yi, J.; Xiong, Y.; Tian, M.; Zhao, Y.-J.; Wang, L. Gate-Tuned Interlayer Coupling in van der Waals Ferromagnet Fe<sub>3</sub>GeTe<sub>2</sub> Nanoflakes. *Phys. Rev. Lett.* **2020**, 125 (4), 047202.
- 40. Gweon, H. K.; Lee, S. Y.; Kwon, H. Y.; Jeong, J.; Chang, H. J.; Kim, K.-W.; Qiu, Z. Q.; Ryu, H.; Jang, C.; Choi, J. W. Exchange Bias in Weakly Interlayer-Coupled van der Waals Magnet Fe<sub>3</sub>GeTe<sub>2</sub>. *Nano Lett.* **2021**, 21 (4), 1672-1678.
- 41. Coey, J. M. D. New permanent magnets; manganese compounds. *J. Phys.: Condens. Matter* **2014**, 26 (6), 064211.
- 42. Baltz, V.; Manchon, A.; Tsoi, M.; Moriyama, T.; Ono, T.; Tserkovnyak, Y. Antiferromagnetic spintronics. *Rev. Mod. Phys.* **2018**, 90 (1), 015005.